



## Effective elastic thickness variations along the Andean margin and their relationship to subduction geometry

**M. Pérez-Gussinyé**

*Group of Dynamics of the Lithosphere, Institute of Earth Sciences "Jaume Almera," CSIC, Lluís Sole i Sabarís s/n, E-08028 Barcelona, Spain (mperez@ija.csic.es)*

**A. R. Lowry**

*Department of Geology, Utah State University, Logan, Utah 84322-4505, USA*

**J. Phipps Morgan**

*Department of Earth Sciences, University of Cornell, 4164 Snee Hall, Ithaca, New York 14853, USA*

**A. Tassara**

*Departamento de Geofísica, Universidad de Chile, Blanco Encalada 2002, Santiago 0000, Chile*

[1] We present a new map of the spatial variations in effective elastic thickness,  $T_e$ , along the Andes estimated using Bouguer coherence. The  $T_e$  variations reflect interactions between subducting slab and preexisting terrane structure. In the forearc, conductive cooling of the continent by the subducting slab exerts primary control on rigidity, resulting in  $T_e$  that is highest ( $\sim 40$  km) where the oceanic lithosphere is oldest and coldest ( $\sim 20^\circ\text{S}$ ). In the central Andes,  $T_e$  is relatively low ( $\sim 20$  km) along the volcanic chain and the Altiplano and Puna plateaus. We interpret this weakening to reflect a high geothermal gradient maintained by advective magmatic processes, a shallow and hot asthenosphere, and a very weak lower crust throughout this region. East of the plateaus, high  $T_e$  delineates underthrusting of the Brazilian shield. Finally, north and south of the plateaus, flat subduction areas are characterized by high  $T_e$ , high shear wave velocity, thick thermal lithosphere, and low heat flow, indicating that continental lithosphere there is thicker, colder, and stronger. On the basis of these relationships we suggest that variations in slab dip along the margin relate to variations in structure of the continental lithosphere. In particular, we propose that upper plate structure influences the width and viscosity of the asthenospheric wedge, which control the suction moment responsible for the subduction angle at depths  $\geq 70$ – $100$  km. For example, when oceanic lithosphere subducts beneath thin continental lithosphere, the low-viscosity asthenosphere allows the slab to detach from the continent and sink into the mantle at normal angles. However, when oceanic lithosphere subducts close or beneath thick and strong continental lithosphere, the asthenospheric wedge narrows and corner flow drags high-viscosity mantle from the base of the thick ( $>150$  km), cold continent into the wedge. Suction forces increase with both narrowing of the wedge and its increasing viscosity. We estimate the asthenospheric viscosity underneath thick, cold continents to be  $\geq 10^{20}$  Pa s, sufficient to induce flat subduction. Later, after prolonged hydration and weakening of the continent's base, asthenospheric flow into the wedge may resume, allowing the slab to sink again into the mantle at normal angles.

**Components:** 13,533 words, 10 figures.

**Keywords:** lithospheric flexure; Andean margin; subduction geometry; continental lithospheric structure.

**Index Terms:** 8138 Tectonophysics: Lithospheric flexure; 8104 Tectonophysics: Continental margins: convergent; 8120 Tectonophysics: Dynamics of lithosphere and mantle: general (1213).

Received 10 August 2007; Revised 10 October 2007; Accepted 15 November 2007; Published 2 February 2008.

Pérez-Gussinyé, M., A. R. Lowry, J. Phipps Morgan, and A. Tassara (2008), Effective elastic thickness variations along the Andean margin and their relationship to subduction geometry, *Geochem. Geophys. Geosyst.*, 9, Q02003, doi:10.1029/2007GC001786.

## 1. Introduction

[2] The Andean Cordillera has resulted from  $\sim 200$  Ma of continuous subduction of oceanic lithosphere beneath the South American continent [Jordan *et al.*, 1983; Isacks, 1988; Allmendinger *et al.*, 1997; Lamb, 2000; Oncken *et al.*, 2006]. Today, the subducting Nazca plate is oldest ( $\sim 48$  Ma) at around  $20^\circ$  S and decreases in age to the north and south (Figure 1). The subducted slab is characterized by a geometry that changes dramatically along strike of the plate boundary. Along most of the margin oceanic lithosphere subducts with a typical geometry, initially dipping  $\sim 5\text{--}30^\circ$  in the megathrust region near the trench before steepening at depths of  $\sim 70\text{--}100$  km into the asthenosphere. Elsewhere slab descends at normal angles until  $\sim 70\text{--}100$  km depth, where the dip shallows to  $<10^\circ$  and follows the base of the continent for hundreds of kilometers inland (Figure 1) [Cahill and Isacks, 1992]. In some instances, the edges of the latter flat style of subduction correspond to aseismic ridges subducting beneath the continent (e.g., the Juan Fernandez and the Nazca ridges in Figure 1). However, not all subducting aseismic ridges spatially correlate with areas where subduction is flat (e.g., the Iquique and Carnegie ridges, Figure 1). Subduction geometry also correlates with present-day volcanic activity. Active calc-alkaline volcanic arcs characterize areas of normal subduction geometry, while flat subduction precludes magmagenesis and hence produces no arc volcanism [Jordan *et al.*, 1983; Ramos, 1999; Gutscher *et al.*, 2000] (Figure 1a).

[3] The cordillera spans 8000 km of the Pacific margin of South America and has elevations of up to 7000 m (Figure 1). It is widest in its central part, near the Arica bend ( $\sim 20^\circ$ S), and narrows to the south and north (Figure 1). The most prominent features of the central Andes are the Altiplano and Puna plateaus, which together comprise the Earth's largest plateau formed in the absence of continent-continent collision [Isacks, 1988; Lamb, 2000] (Figure 1). The plateau has an average elevation of 3800–4500 m and has the greatest crustal thickness of the Andean cordillera (up to 75 km [Yuan *et al.*,

2002]). It is flanked to the west by the Western Cordillera, where the Central Volcanic Zone is located, and to the east by the Eastern Cordillera and Sierras Subandinas, where Neogene to present-day shortening is accommodated (Figure 1b). Areas of recent flat subduction delimit the southern and northern ends of the plateau (Figure 1).

[4] Although commonly equated [e.g., Gutscher *et al.*, 2000], we distinguish here between flat subduction in which the slab reverses its flexural curvature to flatten at  $\sim 100$  km depth and then travels subhorizontally for hundreds of kilometers inland, and shallow-angle subduction in which the slab enters with relatively shallow dip that steepens at  $\sim 70\text{--}100$  km depth, from which point it sinks into the mantle at a normal angle. Shallow-angle subduction is more common (e.g., southern Alaska, Costa Rica, Cascadia, and the Nankai trough) and is associated with the subduction of young or overthickened, buoyant oceanic crust [e.g., Brocher *et al.*, 1994; Gutscher *et al.*, 2000; and references therein]. However, flat subduction is rare, and at present is only well established beneath South America, in central-southern Chile and Peru. It may also occur in northern Colombia, in the Bucaramanga segment, although depth to slab is not well constrained there (see Figure 1). Flat subduction of the Farallon plate under North America may also have occurred during the Laramide orogeny [Jordan *et al.*, 1983]. A recent global compilation of slab depths shows clearly the difference between flat subduction and shallow-angle subduction [see Syracuse and Abers, 2006, Figure 1]. It is worth noting that contemporary flat subduction zones beneath South America and the hypothesized past flat subduction under western North America all involve subduction of typical oceanic lithosphere under large continental landmasses. Most other presently active subduction zones on Earth involve subduction of oceanic lithosphere beneath island arcs or small continental fragments [see Syracuse and Abers, 2006, Figure 1].

[5] Several mechanisms have been proposed for flat subduction, including anomalous buoyancy of the subducting slab due to young lithosphere [Vlaar and Wortel, 1976; Jarrad, 1986] or anom-

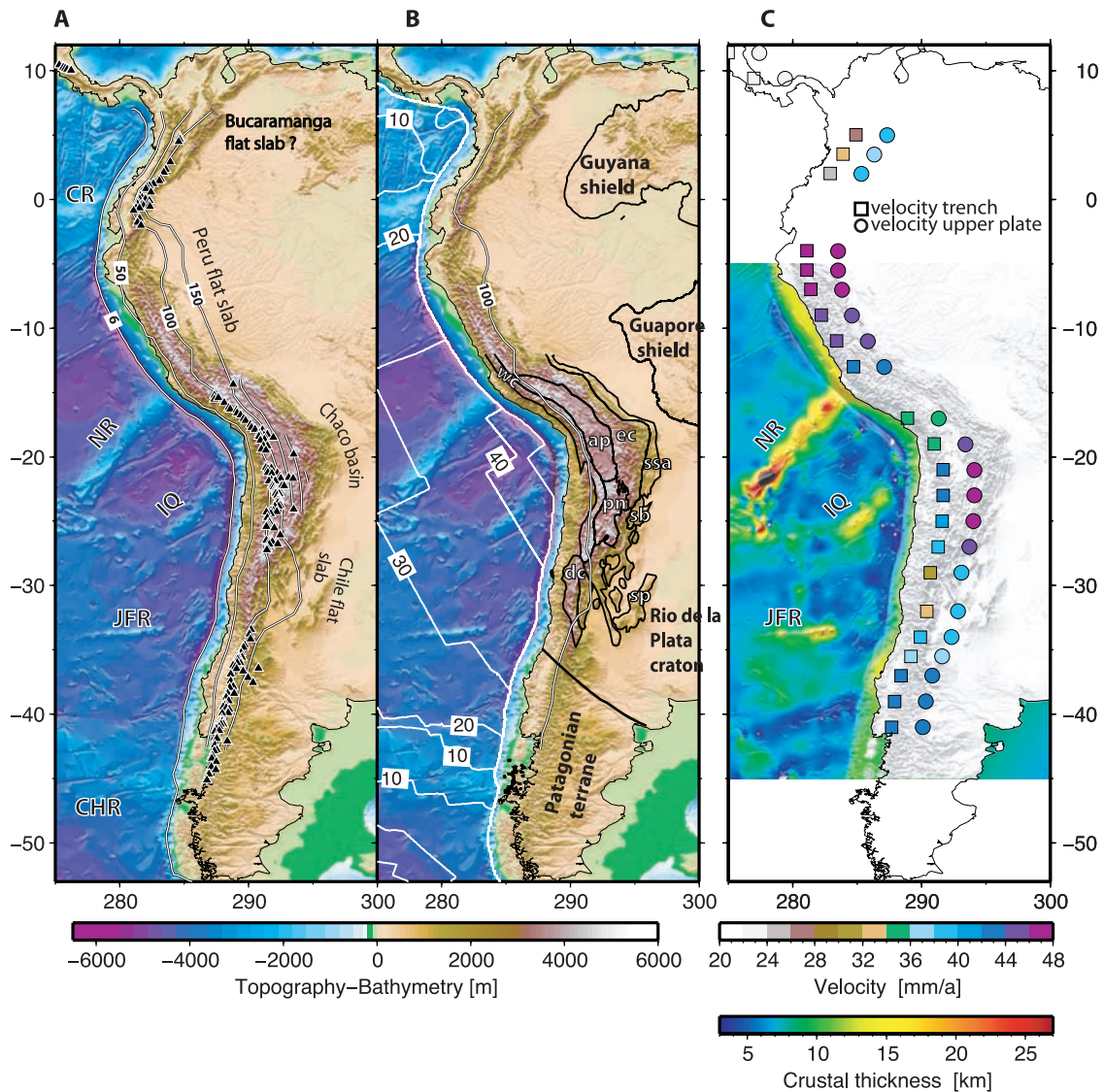


**Figure 1.** (a) Topography and bathymetry of western South America overlain with depth contours to subducting slab (in km) [from *Syracuse and Abers*, 2006] and active volcanoes (triangles). Flat subduction occurs beneath Chile and Peru and perhaps in the Bucaramanga segment. The Chaco basin is found within the Bolivian foreland. Subducting ridges are CR, Carnegie ridge; NR, Nazca ridge; IQ, Iquique ridge; JFR, Juan Fernandez ridge; CHR, Chile ridge. (b) Topography and bathymetry with age contours of oceanic lithosphere and 100 km depth contour of the slab. Main provinces of the Andean cordillera are ap, Altiplano; ec, Eastern Cordillera; dc, Domeyko Cordillera; pn, Puna; sb, Santa Barbara system; ssa, Sierras Subandinas; sp, Sierras Pampeanas; wc, Western Cordillera. Shortening along the Sierras Subandinas occurs by thin-skinned deformation, while north and south of Sierras Subandinas, deformation occurs by thick-skinned fold and thrust belts. Also shown are the largest cratons of the stable platform, the Guapore and Guyana shields, which together form the Brazilian craton and the Rio de la Plata craton. (c) Parameters commonly thought to cause flat subduction are anomalous buoyancy of aseismic ridges (shown here as oceanic crustal thickness) and upper plate velocity [*Gutscher et al.*, 2000; *van Hunen et al.*, 2004]. Oceanic crustal thickness derives from gravity modeling [*Tassara et al.*, 2006]. Thickness of the Iquique ridge (which subducts at normal angle) is similar to that of the Juan Fernandez ridge (where subduction is flat), so ridge buoyancy alone cannot explain flat subduction. Also shown are trench-normal upper plate velocities (circles) and trench-normal velocity after subtracting back-arc deformation rate (squares) from *Lallemand et al.* [2005]. There is no unequivocal relationship between velocity and subduction geometry, even after subtracting back-arc deformation, implying high plate velocity cannot cause flat subduction independent of other factors.

alously thick oceanic crust [Gutscher *et al.*, 2000; Yáñez *et al.*, 2001], rapid trenchward motion of the overriding plate [Vlaar, 1983], and “slab-suction” forces which force the slab to remain attached to the base of the continent [Stevenson and Turner, 1977; Tovish *et al.*, 1978; Hager and O’Connell, 1978].

[6] Suction forces are, in general, not considered necessary for the generation of flat subduction [e.g., van Hunen *et al.*, 2004]. They increase with increasing subduction velocity and asthenospheric wedge viscosity, and also depend on the shape of the asthenospheric wedge [Stevenson and Turner, 1977; Tovish *et al.*, 1978]. Some authors infer that suction should operate similarly in all subduction zones, so it cannot account for observed differences in slab dip [Gutscher *et al.*, 2000]. Numerical experiments with a prescribed asthenospheric wedge shape show that suction forces only appear to be important when the slab has already flattened [van Hunen *et al.*, 2004]. However, the effects of possible variations in shape and viscosity of the asthenospheric wedge resulting from variations in the continental lithospheric structure have not yet been modeled.

[7] In contrast to suction forces, oceanic plateau subduction and the velocity of the overriding upper plate are commonly considered to be important in the generation of flat subduction. However, their relative importance is still a matter of debate. For example, while Gutscher *et al.* [2000] suggest that the primary cause of slab flattening is the subduction of an oceanic plateau, van Hunen *et al.* [2004] show with numerical simulations that flat subduction occurs more easily for a continent overthrusting normal oceanic lithosphere than for a subducting oceanic plateau alone. This is because a subducting plateau should transit from basalt to eclogite at depths of around 70–100 km, and the latter is denser than the mantle, thus negating the slab buoyancy [van Hunen *et al.*, 2004].

[8] Although numerical models show that the high overriding velocity of South America is sufficient to generate flat subduction [van Hunen *et al.*, 2004], this parameter is also unlikely to be the sole cause for flat subduction. For example, a recent compilation of upper plate velocities normal to the South American trench demonstrates no unequivocal correlation between upper plate velocity and subduction geometry: areas of flat subduction have similar or lower velocity than areas subducting at normal angle (Figure 1c [after Lallemand *et al.*, 2005]). This is also the case for the trench velocity, which

Lallemand *et al.* [2005] obtained by subtracting back-arc contraction from the upper plate velocity (Figure 1c).

[9] Hence flat subduction zones in South America do not seem to be generated solely by high rates of trenchward motion of the continent. The spatial correlation of flat subduction zones with subducting aseismic ridges would suggest a role for buoyancy when continental trenchward motion is sufficiently rapid, however not all aseismic ridges in South America give rise to flat subduction. For example, trenchward motion is rapid where the Iquique ridge subducts. The Iquique has dimensions and crustal thickness (and thus buoyancy [Tassara *et al.*, 2006]) similar to the Juan Fernandez ridge, however the subduction angle is normal (Figure 1c). Therefore these proposed mechanisms for flat subduction do not completely explain the process.

[10] An alternative possibility is that the structure of the continent prior to subduction may play a role in controlling the subduction angle. Indeed, there is a strong spatial correlation between morphology of the orogenic belt, which is partly controlled by the inherited upper plate strength variations, and subduction geometry, which importantly affects the strength of the upper plate. It is very possible that inherited strength variations in the upper plate, and those associated with varying subduction dip, feed back on each other resulting in the observed orogenic morphology and subduction dip. It is therefore important to evaluate strength variations in the Andean domain and understand their relationship with normal and flat subduction.

[11] In this paper we present a new map of the effective elastic thickness,  $T_e$ , of the entire Andean cordillera and foreland. Effective elastic thickness is a measure of lithospheric strength, which in turn depends strongly on lithospheric thermal state and composition. Thus  $T_e$  can be viewed as a representation of lithospheric thickness and viscosity [Lowry *et al.*, 2000]. Our  $T_e$  estimates are obtained from multitaper coherence of Bouguer gravity and topography data. We first describe the input data, the resolution of the method and the influence of subduction dynamics on  $T_e$  estimates. Subsequently we present our results and compare them to previous estimates of  $T_e$  along the margin. We then combine these results with other proxies for lithospheric and sub-lithospheric structure to examine how  $T_e$  reflects the thermal and compositional properties of the upper plate. We examine the evidence that these property variations derive from

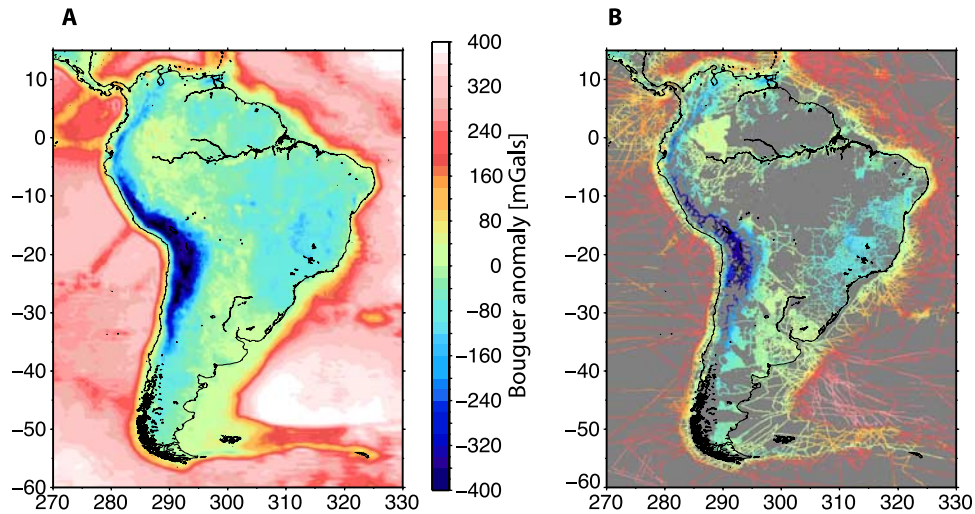


**Figure 2.** Figure 2a shows the Bouguer anomaly used for  $T_e$  estimation. Data were obtained by merging SAGAP data points shown in Figure 2b with the global model EIGEN-CG30C. The latter model has  $1^\circ$  resolution and combines CHAMP and GRACE satellite data with various terrestrial data, including EGM96 [Foerste *et al.*, 2005]. See Pérez-Gussinyé *et al.* [2007] for further explanation.

both subduction-related processes and variations in upper plate structure that predate subduction. We also discuss how variations in upper plate structure may influence the angle of subduction. Finally, we present a conceptual model that explains cycles of flat and steep subduction inferred for the South American margin.

## 2. Input Data

[12] The Bouguer gravity anomaly data used in this study are shown in Figure 2. The Bouguer anomaly combines irregularly distributed Bouguer-corrected gravity measurements compiled by GETECH as part of their South America Gravity Project (SAGP) [Green and Fairhead, 1991] with a Bouguer-corrected version of the EIGEN-CG30C free-air gravity data [Foerste *et al.*, 2005]. The latter data combine free-air gravity from the CHAMP and GRACE satellites with terrestrial free-air gravity from EGM96. The overall accuracy of the EIGEN-CG30C model down to spatial scales of  $\sim 100$  km is estimated to be 8 mGal [Foerste *et al.*, 2005]. Calculation of the Bouguer anomaly from EIGEN-CG30C and combination with the GETECH data are detailed by Pérez-Gussinyé *et al.* [2007].

## 3. Methodology

### 3.1. Bouguer Coherence

[13] To measure the effective elastic thickness  $T_e$ , we model the coherence relating topography and

the Bouguer anomaly, which in combination contain information about the loading and its associated flexural deflection. At short wavelengths, where topographic and internal mass anomalies are uncompensated, Bouguer coherence generally tends to zero. At long wavelengths the response to loading approaches the Airy limit and coherence tends to one [Forsyth, 1985]. The wavelengths at which coherence increases from 0 to 1 depend on load distribution and the effective elastic thickness,  $T_e$ , of the lithosphere. When  $T_e$  is low (i.e., the lithosphere is weak) complete compensation for loading occurs at relatively short wavelengths and vice versa.

[14] To estimate  $T_e$  we compare observed coherence with curves predicted for a range of  $T_e$  values. For each given  $T_e$ , we calculate via deconvolution the surface and sub-surface loads and compensating deflections that reproduce exactly the observed topography and gravity anomaly, an approach first described by Forsyth [1985]. We then calculate a predicted coherence assuming that surface loads (atop the lithosphere) and subsurface loads (within the lithosphere) are statistically uncorrelated [Forsyth, 1985]. The  $T_e$  that minimizes the difference between predicted and observed coherence is the assigned  $T_e$  for an analyzed area. Using this approach, the ratio of surface to subsurface loads, or loading ratio, varies with two-dimensional wave number and is not imposed as an independent parameter as when analytical solutions are calculated. This approach also circumvents spectral bias

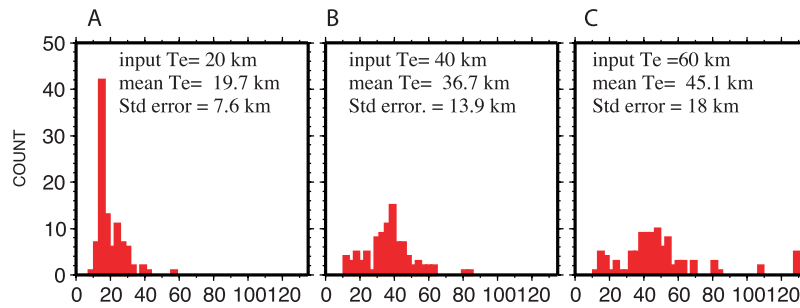


**Figure 3.** Tests with synthetic data demonstrate recovery of  $T_e$  with a window size of  $600 \times 600$  km and multitaper parameters  $NW = 3$ ,  $K = 3$ . Details of the synthetic data generation are given by Pérez-Gussinyé *et al.* [2004]. Results are given for true  $T_e$  of (a) 20, (b) 40, and (c) 60 km. As true  $T_e$  increases, recovery degrades because the ratio of window dimension to flexural wavelength decreases.

effects introduced when power spectral estimates are compared directly to theoretical curves [Pérez-Gussinyé *et al.*, 2004].

[15] Forsyth's [1985] original formulation of the predicted coherence assumed that all internal density variations and loading occur at the Moho. The analysis presented here alternatively assumes loading at mid-crustal levels. Since observed coherence is reproduced equally well by a low  $T_e$  and shallow loading as by a slightly higher  $T_e$  and deeper loading, there is a trade-off between  $T_e$  and assumed depth of loading. However, we tested sensitivity of  $T_e$  estimates to assumed load depth in Europe and found that changing the loading depth from the mid-crust to Moho changed  $T_e$  by  $\sim 5$  km, but the patterns of variations remained the same [Pérez-Gussinyé and Watts, 2005]. We use CRUST2.0 (G. Laske *et al.*, The Reference Earth Model Website, 2000, <http://mahi.ucsd.edu/Gabi/rem.html>) to define the internal density profile. More detailed information on the Bouguer coherence technique used here is given by Pérez-Gussinyé *et al.* [2004, 2007].

### 3.2. Resolution

[16] The coherence function is a normalized cross-power spectrum of the Bouguer gravity and the topography. Hence it involves transformation of the two data sets into the Fourier domain to estimate their auto- and cross-power spectra. Because both data sets are nonperiodic and finite, the Fourier transformation of this windowed data introduces leakage, or transference of power between neighboring frequencies, resulting in estimated spectra that differ from the true spectra. To reduce leakage, the data are tapered prior to Fourier transformation. However, the choice of taper influences the resulting power spectra and hence the

coherence function. Thus the ability to recover  $T_e$  differs depending on the tapering technique used, making it important to understand its limitations.

[17] In this paper, we use Thompson's [1982] multitaper method with Slepian windows [Slepian, 1978]. The spectral estimate obtained with multitapering is a weighted average of spectra generated by a set of individual, orthogonal tapers. Multitapering reduces variance of the spectral estimate and also defines spectral resolution [Percival and Walden, 1993]. The set of orthogonal tapers is defined by setting the bandwidth of the central lobe of the power spectral density of the first-order taper,  $W$ . For a given  $W$ , there are a maximum of  $K = 2NW - 1$  tapers with desirable leakage properties that can be used for the estimation of the spectra, where  $N$  is the number of samples within the data window [e.g., Percival and Walden, 1993; Simons *et al.*, 2000]. Variance of the spectral estimates decreases with the number of tapers used as  $1/K$ , so that the bandwidth and number of tapers are chosen depending on the function under analysis [Percival and Walden, 1993]. We use here a multitaper scheme corresponding to  $NW = 3$ , which is also used in many other studies for  $T_e$  estimation [e.g., Audet and Mareschal, 2004; Pérez-Gussinyé *et al.*, 2004; Pérez-Gussinyé and Watts, 2005]. To optimize lateral resolution over the Andes we use here only the three first-order tapers. Higher-order tapers (in this case the fourth- and fifth-order tapers) upweight the edges of the data window, while lower-order tapers sample the window centre better (see Simons *et al.* [2000] for taper shapes).

[18] In Figure 3 we show  $T_e$  estimates using multitaper parameters  $NW = 3$  and  $K = 3$  on synthetic topography and Bouguer anomaly data generated with a spatially constant  $T_e$  (see Pérez-Gussinyé *et al.* [2004, 2007] on generation of synthetic data).

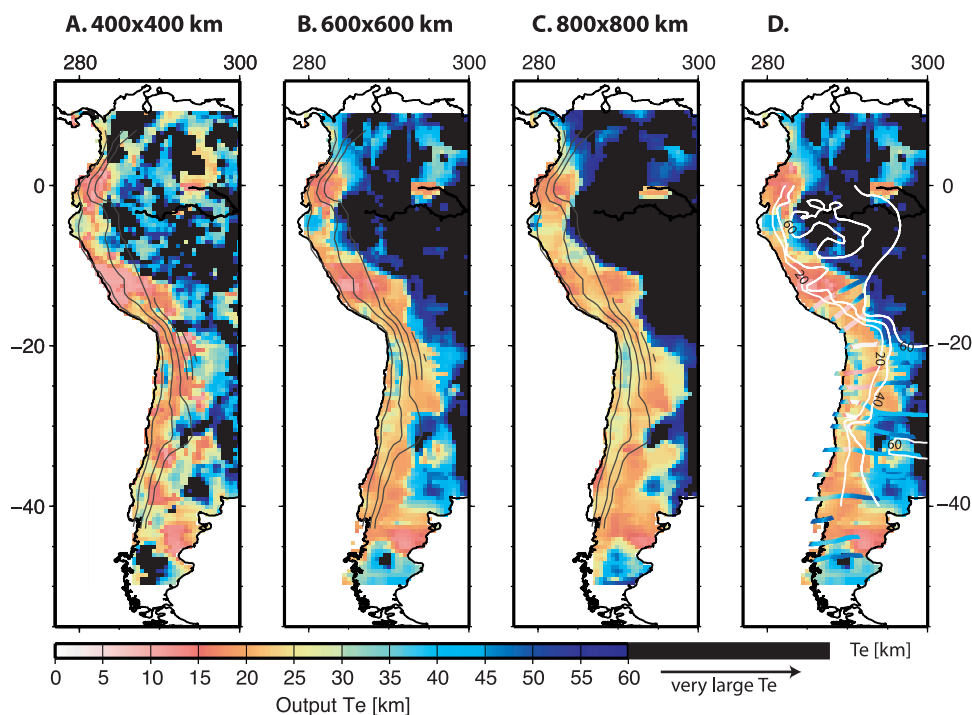


**Figure 4.**  $T_e$  estimates in western South America using (a)  $400 \times 400$  km windows, (b)  $600 \times 600$  km windows, and (c)  $800 \times 800$  km windows. The smallest window yields highly variable  $T_e$  within the stable continental interior, suggesting some spurious variation [Pérez-Gussinyé *et al.*, 2007]. However, the largest window tends to laterally smooth  $T_e$ . We interpret  $600 \times 600$  km as the optimal window size. The  $600 \times 600$  km windows reliably retrieve  $T_e$  up to 60 km, consistent with the range obtained by forward modeling [Tassara, 2005; Stewart and Watts, 1997]. (d) Identical to Figure 4b but superimposed with the estimates from 2-D forward modeling by Tassara [2005] and Stewart and Watts [1997]. Tassara's [2005] estimates are shown along the modeled profiles and color coded with the same color scale as our results. Stewart and Watts [1997] estimates are interpolated between profiles and contoured (white lines). Both forward modeling profiles exhibit low  $T_e$  over the plateaus and high  $T_e$  to the east, as well as high  $T_e$  over flat slab subduction, consistent with coherence analyses presented here.

The tests show that when the flexural wavelength  $\lambda = \pi(4D/\Delta\rho g)^{1/4} \sim 29T_e^{3/4}$  is large relative to the window size, the recovery degrades. Here,  $D$  is flexural rigidity and  $\Delta\rho$  the density difference between mantle and crust (see Swain and Kirby [2003] for derivation). Hence poor recovery results when the flexural wavelength is not adequately sampled within the window and consequently the coherence is low at all wavelengths, resulting in indeterminately high  $T_e$  (Figure 3c). For the  $600 \times 600$  km windows used in Figure 3c, the maximum  $T_e$  that can be recovered with confidence is  $<60$  km.

[19] If  $T_e$  were uniform, larger windows would yield more accurate estimates. However, effective elastic thickness is certain to vary. Since  $T_e$  is assumed constant within the data windows used for estimation,  $T_e$  estimates yield a weighted average of the spatially varying  $T_e$  [Pérez-Gussinyé *et al.*, 2004]. Hence the choice of window size com-

promises between resolution and variance of the resulting estimate. While larger windows are better able to retrieve high  $T_e$ , smaller windows better represent the spatial variations. However, as variance of the spectra increases with decreasing data window size, small windows may yield spurious spatial variations [Pérez-Gussinyé *et al.*, 2004]. To better evaluate these effects, we estimate  $T_e$  with three different window sizes and interpret only those  $T_e$  variations that persist with the three windows.

[20] Figure 4 shows  $T_e$  estimates for western South America using window sizes of  $400 \times 400$  km,  $600 \times 600$  km and  $800 \times 800$  km. Although the general pattern of variation is similar, the mean  $T_e$  increases slightly with window size. The smallest window yields a highly variable  $T_e$  pattern within the continental interior, where  $T_e$  is higher [Pérez-Gussinyé *et al.*, 2007], suggesting some of the  $T_e$  variations may be spurious. The largest window

smoothes the  $T_e$  estimates and probably attenuates real structure. However, all three Figures 4a–4c indicate  $T_e$  is lowest where the Nazca and Carnegie ridges subduct. In the central Andes, between latitudes of  $\sim 28^\circ\text{S}$  and  $\sim 20^\circ\text{S}$ ,  $T_e$  is relatively high in the forearc (west of the 100 km contour of slab depth) and decreases to the east in the Altiplano and Puna plateaus (see Figure 1 and Figure 6 for location). The three estimates also indicate high  $T_e$  west of the plateaus and over the Chilean and northern Peruvian flat slab (Figure 4).

[21] Synthetic tests of the variance (e.g., Figure 3) and resolution [Pérez-Gussinyé *et al.*, 2004, 2007] of  $T_e$  estimation procedures are highly sensitive to parameters assumed in generating the synthetic data, and analyses suggest that some published synthetic tests paint a more negative picture of  $T_e$  recovery than the reality (N. Creati *et al.*, Improved deconvolution of surface and subsurface loads for isostatic analysis, manuscript in preparation, 2008). Comparison of  $T_e$  maps in Figure 4 with South American seismicity, deformation, and other geophysical data suggests much of the structure present in the  $600 \times 600$  km windowed estimates is real, whereas structure in the  $400 \times 400$  km windowed estimates is suspect, and real structures are apparently damped out in the  $800 \times 800$  km windowed estimates [Pérez-Gussinyé *et al.*, 2007]. Consequently we focus on interpreting the  $600 \times 600$  km windowed estimates in the remainder of this paper. The  $600 \times 600$  km windows retrieve  $T_e$  up to 60 km, within the range obtained previously from forward modeling [Tassara, 2005; Stewart and Watts, 1997] (Figure 4d).

### 3.3. Effect of Subduction Zone Dynamics on $T_e$ Estimates

[22] The model of flexural response of a thin plate to mass loading used in estimating  $T_e$  is arguably less valid in a subduction zone than in any other Earth environment. At the forearc, where the upper and lower plate are in contact, the measured effective elastic thickness can be expected to have contributions from both the upper plate and the subducted slab. Since both plates are in contact, a load-induced deflection of one cannot help but exert a significant stress on the other. However, the upper plate and slab cannot behave as a single welded plate owing to the relative motion of the Nazca and South American plates; rather the two components should flexurally decouple like a “leaf-spring” system, in which the two plates

partially relieve strain energy by sliding relative one another at their boundary.  $T_e$  of a leaf spring is approximately the cube root of the sum of cubes of its component  $T_e$ 's [Burov and Diament, 1995], and hence much less than the flexural strength would be if the two behaved as a single welded unit, but nevertheless greater than it would be if the strength reflected only the upper plate.

[23] Behind the forearc region, the upper plate and the slab are decoupled via asthenospheric flow and thus  $T_e$  primarily represents flexural strength of the upper plate. However, slab mass within the asthenosphere will influence the gravity signal, and numerical modeling studies indicate that topography too should be perturbed via flow stress dynamics across the asthenospheric wedge. In the context of  $T_e$  estimation, the primary concern would be that these dynamical effects might significantly alter the coherence of topography and gravity at flexural wavelengths and consequently bias the estimate of lithospheric strength.

[24] We assess here the potential effects of subduction zone dynamics by modeling the approximate amplitude of gravity and topography signals (Figures 5a and 5b) and subtracting them from the total Bouguer anomaly and topography of our data. We then perform Bouguer coherence analysis of the resulting fields to obtain a  $T_e$  that should be unbiased by subduction dynamics. To calculate the gravity perturbation, we use only slab mass anomalies below a depth of 100 km, reasoning that below this depth the slab decouples from the upper plate across the asthenospheric wedge. We used contours of South American slab depth (Figure 1) and assumed a slab density anomaly of  $25 \text{ kg m}^{-3}$  and a 60 km slab thickness to estimate the gravity perturbation. A different choice of density anomaly or thickness would yield results that scale approximately linearly with the change. Dynamic topography was estimated by applying viscous response kernels [Hager and Richards, 1989] to the same slab mass distribution, assuming an asthenospheric viscosity of  $10^{20}$  Pa s. Stresses calculated via the viscous response kernels were then filtered by the flexural response [e.g., Lowry and Zhong, 2003] using a representative estimate of Cordilleran  $T_e \sim 25$  km from this study.

[25] The  $T_e$  variations obtained after subtracting estimates of the slab gravity and dynamic topography fields (Figure 5c) are very similar to those from uncorrected data (Figure 4b), indicating that dynamic effects are negligible. This is because the

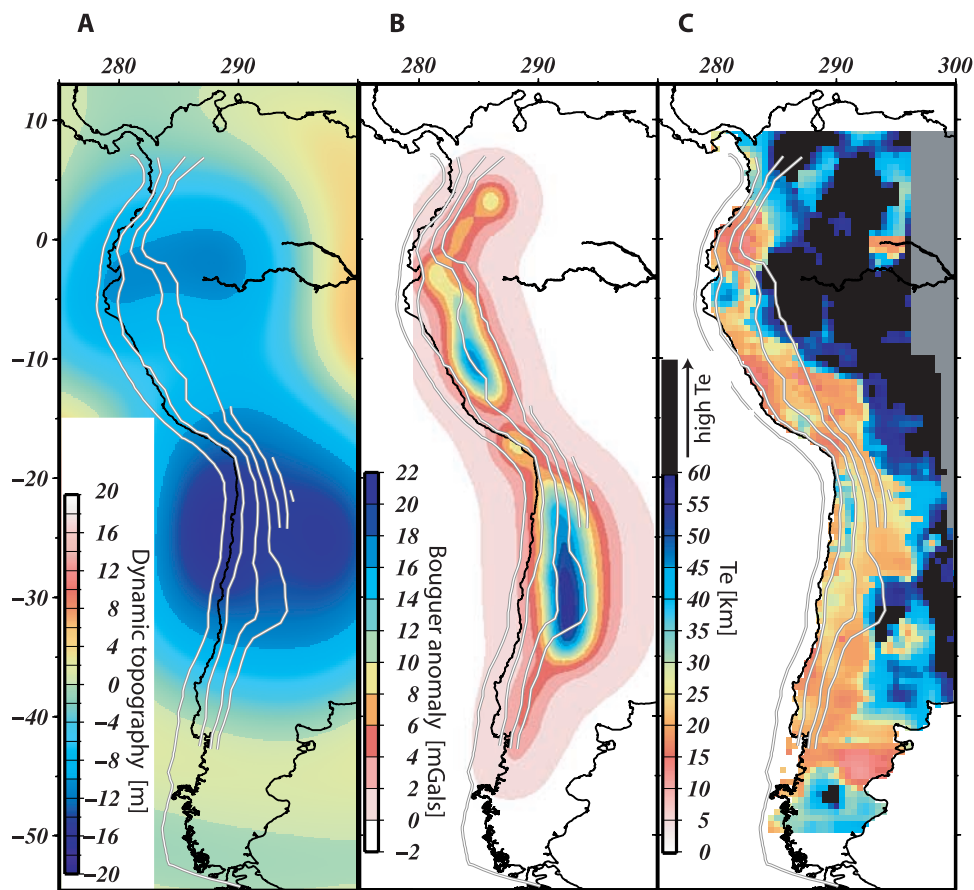


**Figure 5.** Effect of subduction dynamics on  $T_e$  estimates. (a) Estimate of dynamic topography induced by slab below 100 km depth (see section 3.3). (b) Gravity anomaly from slab below 100 km depth. (c)  $T_e$  estimates after subtracting dynamic topography and gravity in Figures 5a and 5b from the observed topography and Bouguer anomaly. These estimates are negligibly different from those in Figure 4b, indicating bias of  $T_e$  estimates by subduction dynamics can be neglected and back-arc  $T_e$  estimates realistically represent strength of continental lithosphere.

dynamic gravity and topography fields have relatively little power at flexural wavelengths, and amplitudes of the measured topography and gravity data are orders of magnitude larger than amplitudes of the corrections. Consequently, the deep slab gravity and topography signals do not significantly change the noise properties in the Bouguer coherence function. Dynamic topography would be more significant using a higher viscosity, but the greater the stress coupling between deep mass and the surface, the less it violates the assumptions of the isostatic model used to estimate  $T_e$ . In fact, the isostatic model assumptions would be least appropriate if there were no topographic expression of the slab gravity. To test possible bias in the event of a lower asthenospheric wedge viscosity, we estimated  $T_e$  for the end-member case in which gravity was corrected for slab mass but topography was assumed to be unperturbed. The resulting  $T_e$  esti-

mates were again negligibly different from those in Figure 4b.

#### 4. Results and Comparison With Previous $T_e$ Estimates Along the Margin

[26] Figure 6 shows the  $T_e$  variations along the Andes resulting from our analysis using  $600 \times 600$  km windows. The first-order pattern is one of relatively high  $T_e$  in the stable continental platform and low  $T_e$  in deforming regions of active subduction. Within the Andean domain,  $T_e$  is relatively high along the forearc and decreases over the Altiplano and Puna. Areas of high  $T_e$  are found behind the plateaus, and nearer to the trench at the Chilean and northern Peruvian flat slab regions.

[27] The general pattern of variation is similar to that obtained by forward modeling 2-D profiles

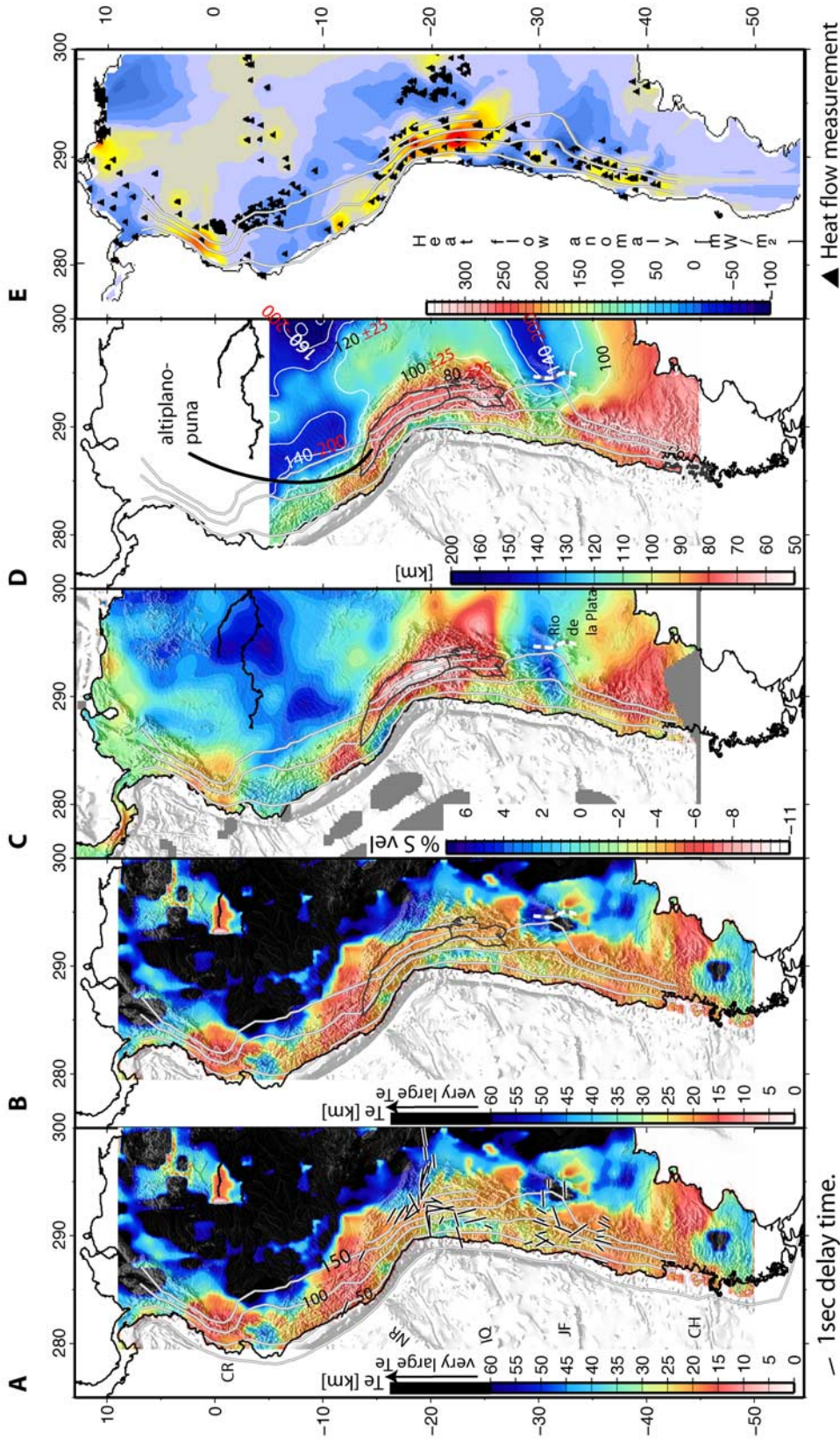


**Figure 6.** (a)  $T_e$  estimates for the Andean domain (as in Figure 4b) and fast directions of shear wave anisotropy in the central Andes and Chilean flat slab segments measured by *Polet et al.* [2000] and *Anderson et al.* [2004], respectively. Seismic anisotropy abruptly changes from east-west to north-south fast directions where  $T_e$  decreases from >50 km to <25 km, indicating  $T_e$  correctly maps changes in lithospheric strength that influence sublithospheric flow. CR, NR, IQ, JF, and CH are abbreviations for aseismic ridges as in Figure 1a. (b)  $T_e$  estimates as in Figure 6a overlain by outline of the Altiplano and Puna plateaus (black lines), the western limit of the Rio de la Plata craton dashed black and white line (note proximity to the Chilean flat slab). (c) Shear wave velocity anomalies at 100 km depth relative to iasp91 from *Feng et al.* [2007]. (d) Thermal boundary layer thickness modeled by *Tassara et al.* [2006]. Black numbers are thicknesses in km presented by *Tassara et al.* [2006]; red numbers represent potential thicknesses taking into account the uncertainties (see section 5). (e) Heat flow anomaly after subtracting a regional heat flow trend generated from measured heat flow using a fourth-order polynomial representation [*Hanza et al.*, 2005]. The regional heat flow field is meant to represent the first-order increase from 60 mW/m<sup>2</sup> in the Stable Platform of South America to 70 mW/m<sup>2</sup> in the Andes. Triangles are measurement locations. All figures include depth contours to the slab from *Syracuse and Abers* [2006].

[Tassara, 2005; Stewart and Watts, 1997] (shown in Figure 4d). Both authors also imaged relatively low  $T_e$  over the Altiplano and Puna, high  $T_e$  behind the plateaus, and high  $T_e$  over the flat slab regions.  $T_e$  variations obtained using wavelet Bouguer coherence [Tassara *et al.*, 2007], however, appear much more laterally smoothed, apparently influenced by the large-scale wavelets used in the analysis [Pérez-Gussinyé *et al.*, 2007]. Indeed synthetic tests indicate that wavelet analysis, although well-suited to retrieving high  $T_e$ , tends to smooth abrupt variations in  $T_e$  (J. F. Kirby and C. J. Swain, An accuracy assessment of the fan wavelet coherence method for elastic thickness estimation, submitted to *Geochemistry, Geophysics, Geosystems*, 2007).

## 5. Discussion

[28] Subduction-related processes modify the thermal and compositional structure and hence flexural rigidity of the upper plate. Therefore one challenge in interpreting  $T_e$  at a subduction zone lies in understanding the relative importance of subduction-related processes versus the inherited thermal and compositional structure of the continental lithosphere in controlling upper plate strength. Subduction-related strength processes include heat mining from the base of the upper plate at depths  $< \sim 100$  km (i.e., where no asthenospheric wedge separates the two plates), advective heating of the upper plate by melts ascending in the volcanic arc, and basal heating and entrainment by asthenospheric wedge flow. At flat subduction zones, the absence of asthenospheric wedge for hundreds of kilometers inland may contribute by cooling and thereby strengthening the upper plate. An additional important process will be the introduction of copious amounts of water to the upper mantle, which can reduce effective viscosity in power law creep by several orders of magnitude [Hirth and Kohlstedt, 1996].

[29] In this section we combine our results with other geophysical data from the cordillera and subduction zone to interpret flexural rigidity of South America's western margin. We focus on how the upper plate lithosphere, as expressed in its modern  $T_e$ , shear wave velocity [Feng *et al.*, 2007], surface heat flow anomaly [Hamza *et al.*, 2005], temperature structure [Tassara *et al.*, 2006], and seismic anisotropy [Polet *et al.*, 2000; Anderson *et al.*, 2004], may influence geometry of the sinking slab and thus tectonic segmentation along the margin.

### 5.1. Forearc Region

[30] The forearc region located between the coast-line and the western Cordillera exhibits variable  $T_e$  from 5 to 40 km (Figure 6 and Figure 1).  $T_e$  is relatively high ( $25 < T_e < 40$  km) throughout most of the forearc, except where the Nazca and Carnegie aseismic ridges intersect the Peru-Chile trench (Figure 6).  $T_e$  is highest ( $\sim 40$  km) at  $\sim 20^\circ\text{S}$  where the slab is oldest. We interpret the high  $T_e$  to reflect combined strength of the upper continental and subducting oceanic lithospheres. The latter strength is controlled by conductive cooling [Watts, 2001], and thus it is greatest where the oceanic lithosphere is coldest and oldest at  $\sim 20^\circ\text{S}$  (compare Figures 1 and 6). Colder subducting lithosphere can also be expected to mine more heat from the base of the continent, contributing further to the total [Tassara, 2005; Yáñez and Cembrano, 2004]. This cooling effect expresses as low  $P$  wave attenuation [Schurr *et al.*, 2006] and low surface heat flow of 20–60 mW/m<sup>2</sup> [Springer, 1999] along the forearc of the central Andes.

### 5.2. Aseismic Ridge Subduction

[31] Within the active deforming region, and along strike of the cordillera, Figure 6 shows  $T_e$  to be low for continental lithosphere affected by subduction of the Nazca and Carnegie ridges (see Figure 1 and Figure 6a). The reason for low  $T_e$  associated with these ridges is not clear. The Carnegie and Nazca ridges consist of thickened oceanic crust along the Galapagos and Easter Island hot spot tracks. The ridges were emplaced on very young oceanic lithosphere. Their emplacement should have perturbed the existing oceanic thermal structure negligibly, so thermal rejuvenation is an unlikely explanation (although surface heat flow at these locations is also anomalously high in Figure 6e). It is also unlikely that the thickness of the ocean crust is sufficient to induce crustal flow and additional flexural decoupling at such shallow depths. One possibility is that brittle-field damage processes associated with subduction of the anomalous bathymetry effectively negate the already-low combined strength residing in the (decoupled) thin upper-plate and subducting oceanic lithospheres elsewhere along the subduction thrust. Brittle-field damage processes may contribute to more efficient advective heat transport in the region as well, thus explaining the high surface heat flow. Evaluating this phenomenon further will require sophisticated numerical modeling, and we will pursue this in future work.

### 5.3. Central Volcanic Zone, Altiplano and Puna Plateaus

[32] Figure 6 shows that, in the central Andes,  $T_e$  decreases from  $\sim 25$ – $45$  km in the forearc to  $\sim 20$  km along the volcanically active Western Cordillera and throughout the Altiplano and Puna. In this segment of the Andes, the slab dips at a normal angle and the volcanic front is located roughly above the 100 km iso-depth contour to the slab (compare Figures 1 and 6). Low  $T_e$  there primarily reflects thermal weakening of the upper plate (both crust and mantle) by advective heat transfer associated with volcanism and also reflects the existence of a very weak lower crust throughout the plateaus [Beck and Zandt, 2002; Haberland et al., 2003; ANCORP Working Group, 2003]. Entrainment and removal of lower lithospheric mantle in the shallow ( $\sim 70$ – $100$  km) asthenospheric mantle wedge beneath the volcanic arc may also contribute to weakening; asthenospheric wedge material probably extends beneath the Altiplano and Puna [e.g., Whitman et al., 1996; Hyndman et al., 2005; Currie and Hyndman, 2006]. The interpretation of an anomalously high geothermal gradient throughout the plateaus is supported by high surface heat flow observed as far inland as the Eastern Cordillera (Figure 6e [after Hamza et al., 2005]), high  $P$  wave attenuation throughout Puna [Schurr et al., 2006], and low shear wave velocity under the Altiplano and Puna at 100 km depth (Figure 6c [after Feng et al., 2007]).

### 5.4. Foreland Region

[33] Along the foreland region, where basins developed by flexure in front of migrating thrust/fold loads in the sub-Andes (e.g., Chaco, Figure 1),  $T_e$  has a wide range of values. In the Bolivian foreland between  $\sim 15^\circ$  and  $\sim 20^\circ$ S we observe high  $T_e$  ( $>40$  km) with an arcuate shape. This area underlies the Eastern Cordillera but not the Altiplano, and it spatially correlates with a longitudinal change in fast directions of seismic shear wave anisotropy from east-west to north-south (Figure 6a [after Polet et al., 2000]). This locale also exhibits an abrupt change in upper mantle  $P$  and  $S$  wave velocities [Dorbath et al., 1993; Feng et al., 2007].

[34] Changes in  $T_e$  along the foreland correlate with changes in style of shortening, as previously noted in  $T_e$  estimates from 1D forward models [Watts et al., 1995; Stewart and Watts, 1997; Tassara, 2005]. High  $T_e$  east of the Altiplano coincides with large amounts of thin-skinned short-

ening. To north and south of this area the foreland lithosphere is weaker, and shortening occurs by thick-skinned tectonics. The high  $T_e$  probably represents Brazilian lithosphere underthrusting the Sierras Subandinas and Eastern Cordillera [Watts et al., 1995; Polet et al., 2000; Beck and Zandt, 2002] in which case the spatial correlation between  $T_e$ , amount of shortening and structural style is causal [Whitman et al., 1996; Kley et al., 1999, Watts et al., 1995]. The strong lithosphere may promote thin-skinned tectonics by underthrusting weaker crust to the west, in which case the large amounts (40–70%) of shortening observed at the surface are limited to a thin zone above a basal décollement [Kley et al., 1999]. South and north of the bend area, weaker foreland lithosphere accommodates contraction on reactivated basement-scale Mesozoic extensional faults, resulting in smaller amounts of shortening (20–35%) in the form of thick-skinned tectonics [Kley et al., 1999; Stewart and Watts, 1997; Whitman et al., 1996].

### 5.5. $T_e$ , Other Proxies for Lithospheric Structure, and Subduction Geometry

[35]  $T_e$  variations along the Andes correlate remarkably well with various proxies for lithospheric structure and, intriguingly, with subduction geometry (Figure 6). Lithosphere above flat subduction displays high  $T_e$ , high shear wave velocity at 100 km depth [Feng et al., 2007], thicker conductive thermal boundary layer [Tassara et al., 2006] and low surface heat flow [Hamza et al., 2005]. Lithosphere above steeply dipping segments generally displays lower  $T_e$ , low shear wave velocity, thinner thermal boundary layer and high heat flow.

[36] Thickness of the conductive thermal boundary layer was estimated as a depth to the  $1300^\circ\text{C}$  isotherm, derived from three-dimensional density modeling of a combination of long-wavelength Bouguer gravity, surface heat flow, tomographic shear wave velocity fields, and petrologic constraints [Tassara et al., 2006]. Despite uncertainties, this parameter complements our estimates of  $T_e$ , which are unresolved above 60 km (see section 3). For example, saturation of the  $T_e$  estimates prevents us from distinguishing apparent differences in strength and thickness of the lithosphere east of flat subduction zones versus east of the Altiplano, which can be resolved with thermal thickness modeling. Taking into account uncertainties, the thermal boundary layer east of the Altiplano is  $100 \pm 25$  km, given  $\pm 20$  mGal error in the gravity data used (and neglecting other parameter error). East of the

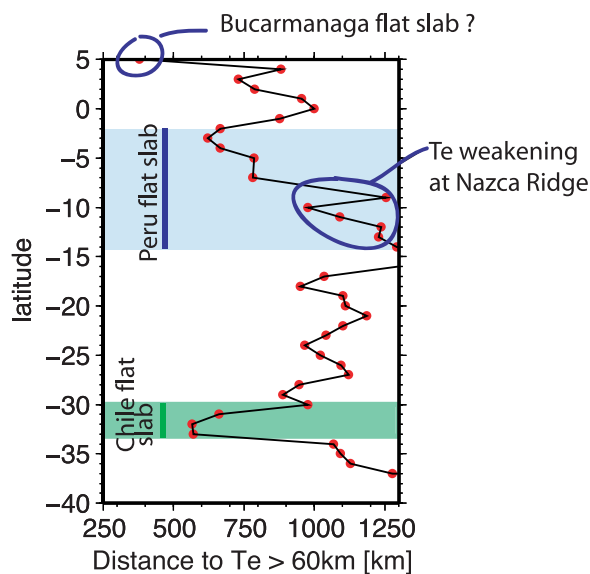


**Figure 7.** Distance from the trench to the nearest point where  $T_e$  exceeds 60 km. Distance is measured longitudinally. High  $T_e$  is nearest the trench at the Chilean and Peruvian flat slabs and the Bucaramana segment in the north, where subduction is not clearly imaged but may also be flat. At the southern part of the Peruvian flat slab segment, distance from the trench to high-strength lithosphere is very large. We believe this is overestimated owing to perturbation of  $T_e$  by subduction of the Nazca ridge (see section 5). Thus high-strength lithosphere generally is nearest the trench at flat subduction segments.

Peruvian and Chilean flat slabs, however, where the thermal boundary layer is thicker  $\sim 140$  km, the depth uncertainty is much larger. Gravity modeling suggests that thermal boundary layer east of the flat slab regions could be up to 200 km and still fit the Bouguer anomaly if a more mafic crustal composition is assumed than in *Tassara et al.* [2006]. A mafic crustal composition is suggested by exposure of mafic rocks immediately east of the Chilean flat slab and with the proximity of the Rio de la Plata craton (Figure 6) [*Tassara et al.*, 2006, and references therein; *Alvarado et al.*, 2007]. Thus thermal boundary layer thickness landward of flat subduction areas is 140 to 200 km, while landward of the Altiplano the thickness is  $100 \pm 25$  km (Figure 6).

[37] The effective elastic thickness also maps changes in lithospheric structure which are accompanied by changes in seismic anisotropy fast axes that reflect sub-lithospheric flow. In the central Andes and Chilean flat slab, abrupt changes in  $T_e$  coincide with sharp changes in the fast direction of shear wave splits (Figure 6a). Fast directions change abruptly from east-west to dominantly

north-south where  $T_e$  decreases from  $>40$  km to  $\sim 20$ – $25$  km. In the Altiplano, *Polet et al.* [2000] interpret east-west directed anisotropy as fossil strain induced by underthrusting of Brazilian lithosphere. North-south anisotropy was interpreted as lateral flow of asthenospheric wedge material along-strike. To the south, in the Chilean flat slab region, east-west directed anisotropy has been interpreted as flow of asthenospheric material out of the wedge as the slab progressively flattened [*Anderson et al.*, 2004]. However, east-west anisotropy could also relate to fossil strain of the overlying continental lithosphere.

[38] Figure 7 shows distance from the trench to the stable continental lithosphere ( $T_e > 60$  km) as a function of latitude. Strong lithosphere is nearest the trench at the Chilean and Peruvian flat slabs and at the Bucaramana segment  $\sim 5^\circ\text{N}$ , where a flat slab has been hypothesized but not yet clearly imaged. At the southern end of the Peru flat slab segment, the distance between the trench and high  $T_e$  is greater. This may be because buoyancy plays a role in subduction geometry on the narrow scale of the Nazca ridge, as suggested by seismic studies for the Chilean flat slab [e.g., *Anderson et al.*, 2007]. However, buoyancy effects cannot explain a large fraction of the flat subduction geometry in South America. Alternatively,  $T_e$  may under-represent deep viscosity in the vicinity of these ridges owing to shallower damage processes associated with the ridge subduction, as noted in section 5.2. Regardless of the reason for the outlier, Figure 7 generally demonstrates the trench to be nearer high  $T_e$  lithosphere where subduction geometry is flat than where the dip is normal.

[39] High  $T_e$  near the trench at regions of flat subduction could be interpreted to result from upper plate cooling by the underlying slab. To investigate how much of the high  $T_e$  above flat subduction regions is due to cooling by the underlying slab, we have calculated the expected  $T_e$  for a range of steady state temperatures and strain rates expected at flat subduction areas (Figure 8). The geotherms assumed steady state cooling of the upper plate by the subducting oceanic plate and were calculated using an analytical expression describing the temperature in the upper plate given by *Molnar and England* [1990]. Assuming shear stresses at the plate interface ranging from 20 to 50 MPa, we obtained geotherms whose temperature at the lithosphere's base spans from  $\sim 850^\circ\text{C}$  to  $1200^\circ\text{C}$ . We also used a geotherm taken from a snapshot of a dynamical model in which flat slab

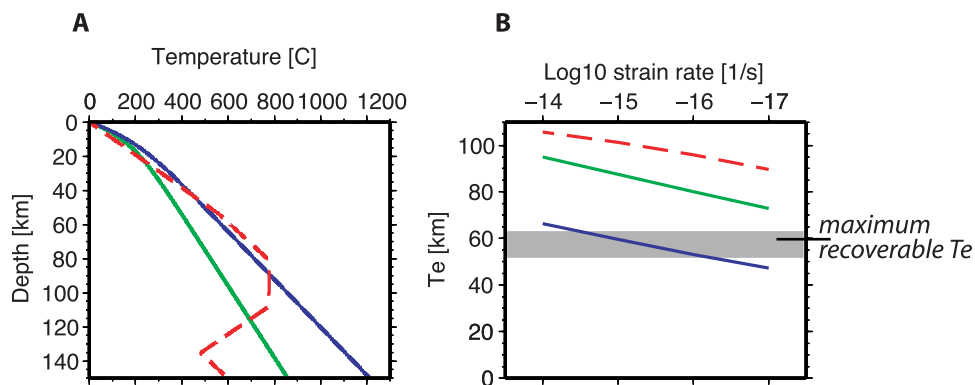


**Figure 8.** (a) Temperature profiles through a 150 km continental upper plate at a flat subduction area in which the upper plate is cooled from below. Blue and green temperature profiles are calculated using a steady state analytical expression [Molnar and England, 1990]. The red dashed geotherm is from a dynamical simulation of flat subduction in South America (J. van Hunen, personal communication, 2007). (b) Calculated  $T_e$  for the temperature profiles shown in Figure 8a and a range of strain rates (color code corresponds to of the geotherms used to calculate  $T_e$  which are shown in Figure 8a). Lower crustal rheology is a medium-strength aggregate, and the mantle consists of wet olivine, giving a lower bound estimate of upper plate strength. The grey line marks the maximum  $T_e$  recoverable with our analysis.

subduction is taking place and is meant to simulate flat subduction in Peru (J. van Hunen, personal communication, 2007) (Figure 8). We found that all of these geotherms are cool enough to yield  $T_e$  much greater than 60 km, which is the maximum  $T_e$  we can recover with the window sizes used for the analysis (Figure 8). Larger windows would not further illuminate this issue, as they would smooth out  $T_e$  variations local to the flat slab (see section 3.2 and Figure 4). Hence  $T_e$  data alone cannot discern whether the high flexural rigidity results from cooling induced by the flat subduction or reflects continental lithosphere which is inherently thicker and stronger prior to subduction.

[40] Thermal boundary layer thickness estimates, however, can help to distinguish between these hypotheses. Tassara *et al.*'s [2006] results suggest the thermal boundary layer is thicker above and landward of the flat subduction zones than over steeply dipping slab (Figure 6). That the thicker thermal boundary layer continues far to the east of any reasonable expectation of thermal cooling due to the flat slab suggests the variations in  $T_e$  and other proxies for lithospheric structure predate the subduction dynamics. Also, the geotherms used in these calculations assume a steady state. However, the Chilean flat slab only flattened 2–5 Ma ago [Ramos *et al.*, 2002], so there the geotherm is probably unrealistically cold, and preexisting strength may be required to explain the high measured  $T_e$ . In the next section we explore how the inherited structure of the continent may exert an influence on geometry of the slab.

## 5.6. Upper Plate Structure and Subduction Geometry

[41] In general, the angle at which subduction occurs in the depth range of 100 to ~200 km reflects a balance between negative buoyancy of the slab, elastic resistance of the slab to change the angle of subduction, and nonhydrostatic pressure forces induced by subduction-driven flow within the asthenosphere (Figure 9). The latter force, known as suction force, acts to prevent the slab from sinking into the mantle, and its magnitude increases with increasing subduction velocity and narrowness and viscosity of the mantle wedge [Stevenson and Turner, 1977, Tovish *et al.*, 1978].

[42] When oceanic lithosphere subducts beneath a continent, the width and viscosity of the wedge is likely to vary as a function of thickness of the overlying continental lithosphere. For example, when an oceanic slab subducts beneath a thin continental lithosphere, the underlying low-viscosity asthenosphere allows the slab to detach from the continent's base and sink at a normal angle into the mantle (Figure 10a). However, if subduction occurs near a thick (>150 km) continental lithosphere, a space problem arises. The asthenospheric wedge is narrower, and viscosity within the wedge may increase as corner flow feeds the wedge with higher-viscosity mantle entrained from beneath the base of the thick continent (Figure 10b). Narrowing of the wedge, e.g., by active subduction erosion of the Andean margin tip [von Huene *et al.*, 2004; Clift and Vannucchi, 2004; Kukowski and Oncken, 2006]

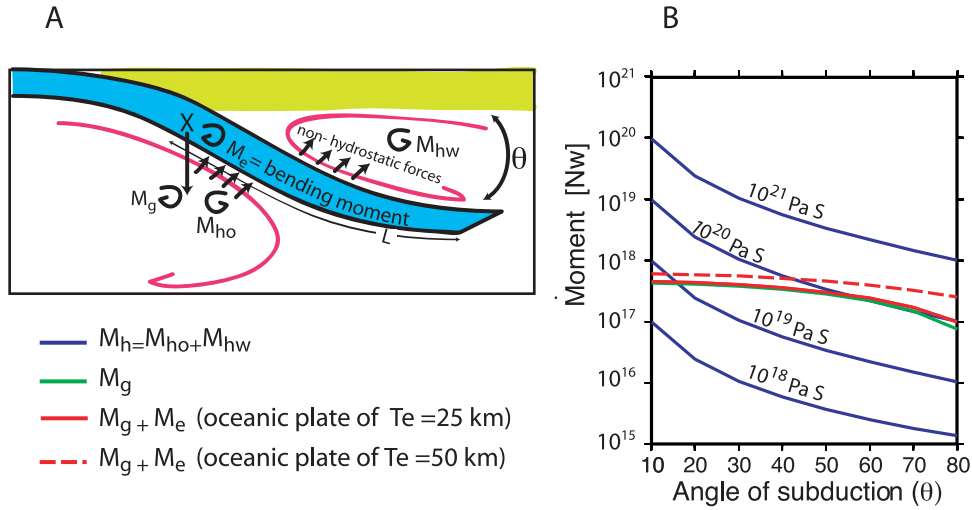


**Figure 9.** (a) Cartoon shows the moments acting on subducting slab.  $M_g$  is the moment due to the negative buoyancy of the slab, which pulls it vertically down.  $M_e$  describes the flexural resistance of the slab to a change in angle of descent.  $M_{ho}$  and  $M_{hw}$  are moments due to the nonhydrostatic pressure forces generated by asthenospheric flow in the oceanic and the wedge corners, respectively.  $L$  is length of the slab used to calculate the moments in section 5.6. (b) Blue curves are moments due to nonhydrostatic pressure forces for different wedge viscosities and wedge corner angles,  $\theta$ . Green curve is the gravity moment; solid red curve is the gravity moment plus flexural moment for an oceanic lithosphere with  $T_e = 25$  km. Dashed red curve is the same for  $T_e = 50$  km. Given an asthenospheric wedge viscosity of  $10^{20}$  Pa s, nonhydrostatic pressure forces will pull the slab toward the base of the continent if the angle of subduction is less than  $40^\circ$ .

and/or high absolute plate velocity of the South American continent, will result in larger suction forces, inducing flat subduction (Figure 10c).

[43] Figure 9b illustrates the dependence of the moments arising from nonhydrostatic pressure forces on the angle of subduction and viscosity of the asthenospheric wedge. This dependence can be derived from the two stream functions describing asthenospheric flow in the wedge and oceanic sides of the slab [Stevenson and Turner, 1977], and is given by

$$M_h = \int [P_{ho}(\theta) - P_{hw}(\theta)] r dr$$

$$= 2VL \left[ \frac{\mu_o \sin \theta}{(\pi - \theta) + \sin \theta} + \frac{\mu_w \sin^2 \theta}{\theta^2 - \sin^2 \theta} \right]$$

where  $P_{ho}(\theta)$  and  $P_{hw}(\theta)$  are nonhydrostatic pressure stress in the oceanic and wedge corners,  $\theta$  is the angle of subduction,  $r$  is distance along the slab,  $L = 200$  km is slab length measured from point X in Figure 9a, and  $V$  is subduction velocity. The viscosities  $\mu_o = 10^{18}$  Pa s and  $\mu_w$  are those for sub-oceanic and wedge corner asthenospheres (Figure 9a), which are assumed to be Newtonian fluids. The asthenospheric viscosity in the oceanic side is meant to represent normal oceanic asthenosphere [Phipps Morgan et al., 2007, and references

therein] and is held constant during the calculations since only the wedge asthenosphere viscosity changes in our scenario. Since the trench is assumed to be static we use the actual convergence velocity between the Nazca and South American plates as the subduction velocity,  $V = 8$  cm/a. Both oceanic and wedge hydrostatic pressure forces exert a counter-clockwise moment,  $M_{ho}$  and  $M_{hw}$  respectively, that act to push the slab against the upper plate (Figure 9a). A greater viscosity  $\mu_o$  in the oceanic corner would increase the moment,  $M_{ho}$ , at high angles and only significantly for wedge viscosities  $\mu_w \leq \mu_o$ .

[44] For flat subduction to occur, the suction moment has to overcome the moment due to gravitational pull on the slab and the elastic moment that resists bending of the slab beneath the continent. The gravity moment is given by

$$M_g = \frac{1}{2} Lgh\Delta\rho \cos \theta$$

where  $g$  is the acceleration of gravity,  $\Delta\rho = 40$  kg/m<sup>3</sup> is density contrast between the slab and surrounding mantle [Afonso et al., 2007],  $h$  is the slab thickness (55–60 km for the slab age of 25–35 Ma at flat-slab segments) and other parameters are as defined above.

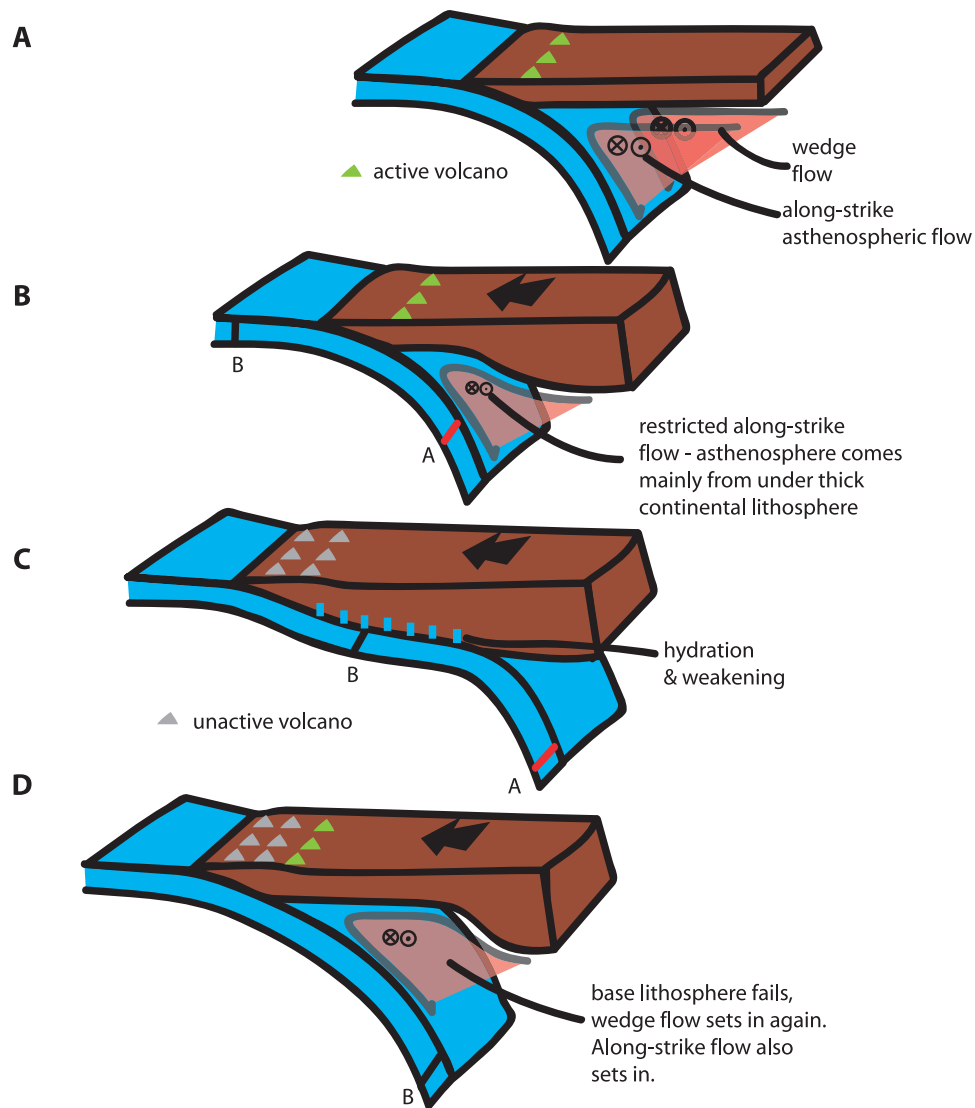


**Figure 10.** Cartoon of various scenarios for subduction of oceanic lithosphere beneath a continent. (a) When oceanic lithosphere subducts beneath thin continental lithosphere, the low-viscosity asthenospheric wedge allows slab subduction to occur at a normal angle. Asthenospheric material is fed into the wedge by corner flow and perhaps by asthenospheric flow along the strike of the wedge, as suggested by *Polet et al.* [2000] for the Altiplano region. (b) When oceanic lithosphere subducts near thick continental lithosphere, the asthenospheric wedge is narrower and restricts lateral flow of low-viscosity asthenosphere. Asthenospheric flow into the wedge entrains mantle from beneath thick, cold continental lithosphere. Asthenospheric viscosity at the base of thick continental lithosphere may be one to three orders of magnitude higher than that of normal subduction wedge mantle, thus increasing wedge viscosity. Combined effects of higher viscosity and narrowing of the asthenospheric wedge increase upward suction moment. (c) Rapid trenchward motion of the continent and/or subduction-erosion bring thick continental lithosphere near enough to the slab to force flat subduction. As the continent moves trenchward, arc volcanism moves inland. With flat subduction, volcanism shuts down. Over time, hydration weakens the base of the continental lithosphere. (d) Weakening of the base of the continental lithosphere promotes detachment of the slab, enabling flow of hot, low-viscosity asthenosphere back into the developing wedge between the slab and continental lithosphere and subduction at a normal angle. Note that we envisage that flat slab does not develop by “swinging upward” and stretching the slab, but rather that the advancing slab simply does not unbend and drop downward into the asthenosphere. This means that sections of the slab that are within the asthenosphere (e.g., section A in Figure 10b) will not change geometry and swing upward to generate flat subduction. Instead, the sections of the slab which are not yet at asthenospheric levels (section B in Figure 10b) will be the ones that acquire a flat geometry as they subduct (section B in Figure 10c). The elastic bending moment required to induce flat subduction in this scenario is smaller than that required to swing the slab upward, making flat subduction occur more easily.

[45] The elastic moment describes the resistance of the slab to a change in curvature where it flattens under the continent. The bending moment that describes resistance of the slab to a change in dip can be expressed as

$$M_e = CD$$

where  $C = 10^{-7} \text{ m}^{-1}$  is the plate curvature associated with slab flattening under the continent, estimated here from the slab depth contours shown in Figure 6, and  $D$  is the flexural rigidity of the lithosphere. For an oceanic lithosphere in the age range between 25 to 35 Ma (as those beneath the Andean flat subduction zones), this flexural rigidity corresponds to a range in effective elastic thicknesses between 25–50 km [Watts, 2001].

[46] Figure 9 demonstrates that when wedge viscosity is  $\geq 10^{20} \text{ Pa s}$ , subduction of a slab at angles less than  $\sim 40^\circ$  can result in a suction moment greater than the sum of the gravitational and bending moments, which would prevent detachment of the slab from the base of the continental lithosphere and so induce flat subduction (Figure 10c).

[47] Conceptually, we expect that as thick continental lithosphere approaches the trench, asthenospheric wedge flow will entrain mantle from near the base of the thick continent, and the wedge will acquire material properties of sub-continental asthenosphere. Important differences between “normal” subduction wedge asthenosphere and asthenosphere below thick, stable continental lithosphere include temperature and water content. Standard conductive geotherms indicate that the temperature at 150 km depth is  $\sim 300^\circ\text{--}400^\circ\text{C}$  colder under stable continental lithosphere than in tectonically active areas such as long-lived asthenospheric wedges [e.g., Ranalli, 1995; Reston and Phipps Morgan, 2004]. Moreover, xenolith and other evidence indicate that subduction introduces copious amounts of water, whereas mantle at the base of stable continental lithosphere ( $>150 \text{ km}$  depth) is comparatively dry [e.g., Dixon *et al.*, 2004]. Modeling of Pleistocene lake rebound [Bills, 1994; Bills *et al.*, 2007] and recent alpine deglaciation [Larsen *et al.*, 2004] indicates viscosity of  $\sim 10^{18}\text{--}10^{19} \text{ Pa s}$  in regions of recent or active subduction, whereas asthenospheric viscosity of  $10^{20}\text{--}10^{21} \text{ Pa s}$  is required for postglacial rebound under stable continental lithosphere [Bergstrand *et al.*, 2005; Peltier and Jiang, 1996]. If asthenosphere from beneath thick continental lithosphere is entrained into wedge flow, and diffusion of slab-derived water is not sufficiently rapid to immedi-

ately hydrate the wedge, viscosities  $\geq 10^{20} \text{ Pa s}$  required for flat subduction may be attained.

## 5.7. Cycles of Subduction Beneath Continental Lithosphere

[48] The results presented here enable us to hypothesize the following scenarios for subduction of oceanic lithosphere beneath continents:

[49] 1. When oceanic lithosphere subducts beneath thin continental lithosphere, the underlying low-viscosity asthenosphere allows the slab to detach from the continent’s base and sink into the mantle at normal angles (Figure 10a), as observed in the central Andes. Polet *et al.* [2000] suggest that north-south directed anisotropy there indicates lateral flow of asthenospheric material along the subduction wedge. This hypothesis is consistent with  $T_e$  and other geophysical data presented here, and we speculate that this flow is important for maintaining a low-viscosity asthenospheric wedge (Figure 10a).

[50] 2. When oceanic lithosphere subducts near thick continental lithosphere, the asthenospheric wedge narrows. Wedge flow would entrain mantle from beneath the thick and cold continental lithosphere. Mantle viscosity beneath stable continental lithosphere may be an order of magnitude or more greater than that of typical asthenospheric wedge. The combined effect of higher wedge viscosity (entrained from beneath continental lithosphere) and progressive narrowing of the asthenospheric wedge (by trenchward motion of the continent) leads to an increase in suction forces (Figure 10b).

[51] 3. Either rapid trenchward motion of the continent or high levels of subduction-erosion at the front, as is the case for South America, brings the thick continental lithosphere close enough to the trench for flat subduction to ensue (Figure 10c). As the continent moves toward the oceanic plate, the active volcanic chain moves inland. When flat subduction is achieved, the asthenospheric wedge disappears and volcanism ceases (Figure 10c). This would correspond to the present-day situation in the Chile and Peru flat slab segments.

[52] With time, dehydration of the oceanic slab weakens the base of the continental lithosphere (Figure 10c). Slab dehydration occurs at all depths during subduction, but it is least efficient at depths greater than  $\sim 100 \text{ km}$  [Rüpkke *et al.*, 2004] where hydration and weakening of continental mantle lithosphere will be slow. This may explain why continental lithosphere above the Chilean flat slab

still exhibits a dry signature [Wagner *et al.*, 2006], where the slab flattened only 2–5 Ma [Ramos *et al.*, 2002]. Prolonged Laramide flat slab subduction may have hydrated and weakened previously stable lithosphere in western North America, where Archean-aged lithosphere under the present Basin and Range is now hydrated, weak and thin [Lee, 2005; Dixon *et al.*, 2004]. Numerical simulations further support the hypothesis that slab dehydration may facilitate significant thinning of the upper plate [Arcay *et al.*, 2006].

[53] 4. Finally, weakening of the continental lithosphere leads to its failure, allowing the slab to decouple from the continental lithosphere and sink into the asthenosphere, and enabling flow of hot, low-viscosity asthenosphere back into the space between the slab and overriding plate (Figure 10d).

[54] Figures 10b to 10d can be viewed as an evolutionary model, representing how upper plate structure coupled with its trenchward motion combine to promote repeated cycles of flat and normal subduction over time. Geochemical analyses of volcanic rocks in northern Chile (21°–26°S) have been used to hypothesize repeated cycles of steep and flat subduction since 200 Ma, in which 30–40 million year periods of normal subduction are punctuated by shorter 5–12 million years flat subduction episodes [Haschke *et al.*, 2007]. Such cyclical behavior would be a natural consequence of the subduction of oceanic lithosphere beneath variable-thickness continental lithosphere proposed here.

[55] In the case of the Altiplano, hypothesized Eocene-Oligocene flat subduction [Haschke *et al.*, 2007; Isacks, 1988] would have occurred when trenchward encroachment of the continent brought thick Brazilian lithosphere near enough to the trench to shut down wedge flow (i.e., Figure 10b to 10c). The modern Altiplano lithosphere would represent a remnant of the original lithosphere after hydration, weakening, and orogenic contraction (Figure 10d). The Chilean and Peruvian flat slab segments would represent a different stage in the same process, in which thick continental lithosphere is near enough and moving fast enough relative to the trench to induce flat subduction (Figure 10c).

## 6. Conclusions

[56] We have estimated effective elastic thickness  $T_e$  of the western margin of South America using Bouguer coherence analysis of isostatic response and a multitaper technique. Our results show a first-order pattern of relatively high  $T_e$  in the stable

continental platform and low  $T_e$  in deforming regions of active subduction. In general,  $T_e$  correlates very well with other proxies for lithospheric structure. Low  $T_e$  correlates with low shear wave velocity at 100 km depth, thin thermal boundary layer and high heat flow.

[57]  $T_e$  varies along- and across-strike of the Andean margin. Along the forearc, where the oceanic and continental lithosphere are in contact,  $T_e$  increases from 25–40 km, and it is highest at around 20°S, where the oceanic lithosphere is oldest. We interpret this to indicate that cooling of the upper plate by the oceanic lithosphere controls the rheological strength of the system.

[58] Our results show that  $T_e$  decreases from the forearc to the volcanic arc and remains low over the Altiplano and Puna. We interpret this weakening to reflect a high geothermal gradient owing to advective magmatic processes, a hot and shallow asthenosphere that continues as far inland as the eastern edge of the plateaus, and weakening related to the very thick, felsic and partially molten lower crust of the plateaus.

[59] Foreland lithosphere beneath the central Andes is strong and probably reflects underthrusting of the Brazilian lithosphere under the Eastern Cordillera and Sierras Pampeanas, where shortening by thin-skinned tectonics is ongoing. Immediately to the south and north, the foreland lithosphere is weak and shortening occurs by thick-skinned tectonics. These results reinforce those obtained previously from one-dimensional modeling of selected profiles in the central Andean foreland by Watts *et al.* [1995] and Stewart and Watts [1997]. We follow these authors as well as Whitman *et al.* [1996] and Kley *et al.* [1999] in suggesting that the style and amount of foreland deformation is controlled by strength of the foreland lithosphere.

[60] Finally,  $T_e$  correlates with slab geometry. Areas where subduction is flat exhibit high  $T_e$  nearer the trench than those with normal subduction. Flat subduction segments and their eastward projections also exhibit thicker thermal boundary layer, higher shear wave velocity and lower heat flow than normally dipping segments. These observations in combination indicate that flat subduction is characterized by the presence of thick, strong and cold continental lithosphere nearer the trench than where normal subduction is observed. On the basis of these observations, we suggest that variations in slab geometry along the South American

margin relate to variations in the structure of the upper plate. In particular, we propose that upper plate structure influences the width and viscosity of the asthenospheric wedge, which in turn controls the suction moment responsible for maintaining slab attachment to the base of the continental lithosphere at depths greater than 70–100 km.

[61] When an oceanic lithosphere subducts beneath thin continental lithosphere, the underlying asthenospheric wedge is wide and has low viscosity, allowing the slab to detach from the continental lithosphere and sink into the mantle at normal angles (e.g., the central Andes). However, when the slab nears thick continental lithosphere, the asthenospheric wedge narrows and corner flow entrains higher-viscosity asthenospheric mantle from beneath the thick (>150 km), cold continental lithosphere. Narrowing of the wedge and its increased viscosity lead to an increase in suction forces. We expect that dry asthenospheric viscosity beneath thick (>150 km), cold continents may exceed  $\sim 10^{20}$  Pa s. A moment balance calculation suggests that such a high wedge viscosity would be sufficient to induce flat subduction. Our conceptual model, coupled with trenchward motion of the South American continent, can account for hypothesized cycles of normal and flat subduction inferred for the margin. The extent to which continental lithospheric structure may influence the geometry of the slab will be a focus of future research using dynamical models.

## Acknowledgments

[62] We thank Rob Govers and an anonymous reviewer for their comments on the manuscript, which helped improve the work presented here. We also thank Marcelo Assumpcao, Mei Feng, and Suzan Goes for providing the shear wave velocity data shown here and Valiya Hamza for providing the heat flow anomaly map. We thank Jeroen van Hunen for providing estimates of the upper plate geotherm at a flat subduction zone. M. Pérez-Gussinyé was funded under a RyC contract of the Spanish Ministry of Science and Education.

## References

Afonso, J. C., G. Ranalli, and M. Fernández (2007), Density structure and buoyancy of the oceanic lithosphere revisited, *Geophys. Res. Lett.*, *34*, L10302, doi:10.1029/2007GL029515.

Allmendinger, R. W., T. E. Jordan, S. M. Kay, and B. L. Isacks (1997), The evolution of the Altiplano-Puna Plateau of the Central Andes, *Annu. Rev. Earth Planet. Sci.*, *25*, 139–174.

Alvarado, P., S. Beck, and G. Zandt (2007), Crustal structure of the southern-central Andes Cordillera and backarc region from waveform modeling, *Geophys. J. Int.*, doi:10.1111/j.1365-246X.2007.03452.x.

ANCORP Working Group (2003), Seismic imaging of a convergent continental margin and plateau in the central Andes (Andean Continental Research Project 1996 (ANCORP'96)), *J. Geophys. Res.*, *108*(B7), 2328, doi:10.1029/2002JB001771.

Anderson, M. L., G. Zandt, E. Triep, M. Fouch, and S. Beck (2004), Anisotropy and mantle flow in the Chile-Argentina subduction zone from shear wave splitting analysis, *Geophys. Res. Lett.*, *31*, L23608, doi:10.1029/2004GL020906.

Anderson, M. L., P. Alvarado, S. Beck, and G. Zandt (2007), Geometry and brittle deformation of the subducting Nazca plate, central Chile and Argentina, *Geophys. J. Int.*, *171*(1), 419–434, doi:10.1111/j.1365-246X.2007.03483.x.

Arcay, D., M.-P. Doin, E. Tric, R. Bousquet, and C. de Capitani (2006), Overriding plate thinning in subduction zones: Localized convection induced by slab dehydration, *Geochem. Geophys. Geosyst.*, *7*, Q02007, doi:10.1029/2005GC001061.

Audet, P., and J.-C. Mareschal (2004), Variations in elastic thickness in the Canadian Shield, *Earth Planet. Sci. Lett.*, *226*, 17–31.

Beck, S. L., and G. Zandt (2002), The nature of orogenic crust in the central Andes, *J. Geophys. Res.*, *107*(B10), 2230, doi:10.1029/2000JB000124.

Bergstrand, S., H. G. Scherneck, G. A. Milne, and J. M. Johansson (2005), Upper mantle viscosity from continuous GPS baselines in Fennoscandia, *J. Geodyn.*, *39*(2), 91–109.

Billen, M. I., and G. Hirth (2005), Newtonian versus non-Newtonian upper mantle viscosity: Implications for subduction initiation, *Geophys. Res. Lett.*, *32*, L19304, doi:10.1029/2005GL023457.

Bills, B. G. (1994), Viscosity estimates for the crust and upper mantle from patterns of lacustrine shoreline deformation in the eastern Great Basin, *J. Geophys. Res.*, *99*(B11), 22,059–22,086.

Bills, B. G., K. D. Adams, and S. G. Wesnousky (2007), Viscosity structure of the crust and upper mantle in western Nevada from isostatic rebound patterns of the late Pleistocene Lake Lahontan high shoreline, *J. Geophys. Res.*, *112*, B06405, doi:10.1029/2005JB003941.

Brocher, T., G. S. Fuis, M. A. Fisher, G. Plafker, and M. J. Moses (1994), Mapping the megathrust beneath the northern Gulf of Alaska using wide-angle seismic data, *J. Geophys. Res.*, *99*, 11,663–11,685.

Burov, E. B., and M. Diament (1995), The effective elastic thickness of continental lithosphere: What does it really mean?, *J. Geophys. Res.*, *100*, 3905–3927.

Cahill, T., and B. Isacks (1992), Seismicity and shape of the subducted Nazca plate, *J. Geophys. Res.*, *97*, 17,503–17,529.

Clift, P., and P. Vannucchi (2004), Controls on tectonic accretion versus erosion in subduction zones: Implications for the origin and recycling of the continental crust, *Rev. Geophys.*, *42*, RG2001, doi:10.1029/2003RG000127.

Currie, C. A., and R. D. Hyndman (2006), The thermal structure of subduction zone back arcs, *J. Geophys. Res.*, *111*, B08404, doi:10.1029/2005JB004024.

Dixon, J. E., T. H. Dixon, D. R. Bell, and R. Malservisi (2004), Lateral variation in upper mantle viscosity: The role of water, *Earth Planet. Sci. Lett.*, *222*, 451–467.

Dorbath, C., M. Granet, G. Poupinet, and C. Martinez (1993), A teleseismic study of the Altiplano and the Eastern Cordillera in northern Bolivia: New constraints on a lithospheric model, *J. Geophys. Res.*, *98*, 9825–9844.

Feng, M., S. van der Lee, and M. Assumpção (2007), Upper mantle structure of South America from joint inversion of waveforms and fundamental mode group velocities of Ray-

- leigh waves, *J. Geophys. Res.*, *112*, B04312, doi:10.1029/2006JB004449.
- Foerste, C., et al. (2005), A new high resolution global gravity field model derived from combination of GRACE and CHAMP mission and altimetry/gravimetry surface gravity data, paper presented at EGU General Assembly, Eur. Geosci. Union, Vienna.
- Forsyth, D. W. (1985), Subsurface loading estimates of the flexural rigidity of continental lithosphere, *J. Geophys. Res.*, *90*, 12,623–12,632.
- Green, C. M., and J. D. Fairhead (1991), The South American Gravity Project, in *Recent Geodetic and Gravimetric Research in Latin America*, edited by W. Torge, A. Fletcher, and J. Tanner, pp. 82–95, Springer, New York.
- Gutscher, M.-A., W. Spakman, H. Bijwaard, and R. Engdahl (2000), Geodynamics of flat subduction: Seismicity and tomographic constraints from the Andean margin, *Tectonics*, *19*, 814–833.
- Haberland, C., A. Rietbrock, B. Schurr, and H. Brasse (2003), Coincident anomalies of seismic attenuation and electrical resistivity beneath the southern Bolivian Altiplano plateau, *Geophys. Res. Lett.*, *30*(18), 1923, doi:10.1029/2003GL017492.
- Hager, B. H., and R. J. O'Connell (1978), Subduction zone dip angles and flow driven by plate motion, *Tectonophysics*, *50*, 111–133.
- Hager, B. H., and M. A. Richards (1989), Long-wavelength variations in Earth's geoid: Physical models and dynamical implications, *Philos. Trans. R. Soc. London, Ser. A*, *328*, 309–327.
- Hamza, V., F. J. S. Silva Dias, A. J. L. Gomes, and Z. G. Delgadillo Terceros (2005), Numerical and functional representations of regional heat flow in South America, *Phys. Earth Planet. Inter.*, *152*, 223–256.
- Haschke, M., A. Günther, D. Mlenick, H. Echtler, K.-J. Reutter, E. Scheuber, and O. Oncken (2007), Central and southern Andean tectonic evolution inferred from arc magmatism, in *The Andes: Active Subduction Orogeny, Frontiers Earth Sci.*, vol. 1, edited by O. Oncken et al., pp. 337–354, Springer, New York.
- Hirth, G., and D. L. Kohlstedt (1996), Water in the oceanic upper mantle: Implications for rheology, melt extraction and the evolution of the lithosphere, *Earth Planet. Sci. Lett.*, *144*, 93–108.
- Hyndman, D., C. A. Currie, and S. P. Mazzotti (2005), Subduction zone backarcs, mobile belts, and orogenic heat, *GSA Today*, *15*, 4–10, doi:10.1130/1052-5173.
- Isacks, B. (1988), Uplift of the central Andean plateau and bending of the Bolivian orocline, *J. Geophys. Res.*, *93*, 3211–3231.
- Jarrad, R. D. (1986), Relations among subduction parameters, *Rev. Geophys.*, *24*(2), 217–284.
- Jordan, T., B. Isacks, R. W. Allmendinger, J. A. Brewer, V. A. Ramos, and C. J. Ando (1983), Andean tectonics related to geometry of the subducted Nazca plate, *Geol. Soc. Am. Bull.*, *94*, 341–361.
- Kley, J., C. R. Monaldi, and J. A. Salfity (1999), Along-strike segmentation of the Andean foreland: Causes and consequences, *Tectonophysics*, *301*, 75–94.
- Kukowski, N., and O. Oncken (2006), Subduction erosion—The 'normal' mode of fore-arc material transfer along the Chilean margin?, in *The Andes: Active Subduction Orogeny, Frontiers Earth Sci.*, vol. 1, edited by O. Oncken et al., pp. 217–236, Springer, New York.
- Lallemand, S., A. Heuret, and D. Boutelier (2005), On the relationships between slab dip, back-arc stress, upper plate absolute motion, and crustal nature in subduction zones, *Geochem. Geophys. Geosyst.*, *6*, Q09006, doi:10.1029/2005GC000917.
- Lamb, S. (2000), Active deformation in the Bolivian Andes, South America, *J. Geophys. Res.*, *105*, 25,627–25,653.
- Larsen, C. F., R. J. Motyka, J. T. Freymueller, K. A. Echelmeyer, and E. R. Ivins (2004), Rapid uplift of southern Alaska caused by recent ice loss, *Geophys. J. Int.*, *158*(3), 1118–1133.
- Lee, C. A. (2005), Trace element evidence for hydrous metasomatism at the base of the North American lithosphere and possible association with Laramide low-angle subduction, *J. Geol.*, *113*, 673–685.
- Lowry, A. R., and S. Zhong (2003), Surface versus internal loading of the Tharsis rise, Mars, *J. Geophys. Res.*, *108*(E9), 5099, doi:10.1029/2003JE002111.
- Lowry, A. R., N. M. Ribe, and R. B. Smith (2000), Dynamic elevation of the Cordillera, western United States, *J. Geophys. Res.*, *105*(B10), 23,371–23,390.
- Molnar, P., and P. England (1990), Temperatures, heat flux, and frictional stress near major thrust faults, *J. Geophys. Res.*, *95*, 4833–4856.
- Oncken, O., D. Hindle, J. Kley, K. Elger, P. Victor, and K. Schemmann (2006), Deformation of the central Andean upper plate system: Facts, fiction, and constraints for plateau models, in *The Andes: Active Subduction Orogeny, Frontiers Earth Sci.*, vol. 1, edited by O. Oncken et al., pp. 3–28, Springer, New York.
- Peltry, W. R., and X. H. Jiang (1996), Glacial isostatic adjustment and Earth rotation: Refined constraints on the viscosity of the deepest mantle, *J. Geophys. Res.*, *101*(B2), 3269–3290.
- Percival, D. B., and A. T. Walden (1993), *Spectral Analysis for Physical Applications, Multitaper and Conventional Univariate Techniques*, pp. 1–190, Cambridge Univ. Press, New York.
- Pérez-Gussinyé, M., and A. B. Watts (2005), The long-term strength of Europe and its implications for plate forming processes, *Nature*, *436*, 381–384, doi:10.1038/nature03854.
- Pérez-Gussinyé, M., A. R. Lowry, A. B. Watts, and I. Velicogna (2004), On the recovery of effective elastic thickness using spectral methods: Examples from synthetic data and from the Fennoscandian Shield, *J. Geophys. Res.*, *109*, B10409, doi:10.1029/2003JB002788.
- Pérez-Gussinyé, M., A. R. Lowry, and A. B. Watts (2007), Effective elastic thickness of South America and its implications for intracontinental deformation, *Geochem. Geophys. Geosyst.*, *8*, Q05009, doi:10.1029/2006GC001511.
- Phipps Morgan, J., J. Hasenclever, M. Hort, L. Rüpke, and E. M. Parmentier (2007), On subducting slab entrainment of buoyant asthenosphere, *Terra Nova*, *19*(3), 167–173, doi:10.1111/j.1365-3121.2007.00737.x.
- Polet, J., P. G. Silver, S. Beck, T. Wallace, G. Zandt, S. Ruppert, R. Kind, and A. Rudloff (2000), Shear wave anisotropy beneath the Andes from the BANJO, SEDA, and PISCO experiments, *J. Geophys. Res.*, *105*(B3), 6287–6304.
- Ramos, V. A. (1999), Plate tectonic setting of the Andean Cordillera, *Episodes*, *22*, 183–199.
- Ramos, V. A., E. O. Cristallini, and D. J. Pérez (2002), The Pampean flat slab of the central Andes, *J. South Am. Sci.*, *15*, 59–78.
- Ranalli, G. (1995), *Rheology of the Earth*, 2nd ed., 413 pp., Chapman and Hall, London.
- Reston, T. J., and J. Phipps Morgan (2004), The continental geotherm and the evolution of rifted margins, *Geology*, *32*, 133–136.

- Rüpke, L. H., J. Phipps Morgan, M. Hort, and A. D. Connolly (2004), Serpentine and the subduction water cycle, *Earth Planet. Sci. Lett.*, *223*, 17–34.
- Schurr, B., A. Rietbrock, G. Asch, R. Kind, and O. Oncken (2006), Evidence for lithospheric detachment in the central Andes from local earthquake tomography, *Tectonophysics*, *415*, 203–223.
- Simons, F. J., M. T. Zuber, and J. Korenaga (2000), Spatio-spectral localization of isostatic coherence anisotropy in Australia and its relation to seismic anisotropy: Implications for lithospheric deformation, *J. Geophys. Res.*, *105*, 19,163–19,184.
- Slepian, D. (1978), Prolate spheroidal wave functions, Fourier analysis and uncertainty, V, The discrete case, *Bell Syst. Tech. J.*, *57*, 1031–1042.
- Springer, M. (1999), Interpretation of heat flow density in the central Andes, *Tectonophysics*, *306*, 377–395.
- Stevenson, D. J., and S. J. Turner (1977), Angle of subduction, *Nature*, *270*, 334–336.
- Stewart, J., and A. B. Watts (1997), Gravity anomalies and spatial variations of flexural rigidity at mountain ranges, *J. Geophys. Res.*, *102*, 5327–5352.
- Swain, C. J., and J. F. Kirby (2003), The effect of ‘noise’ on estimates of the elastic thickness of the continental lithosphere by the coherence method, *Geophys. Res. Lett.*, *30*(11), 1574, doi:10.1029/2003GL017070.
- Syracuse, E. M., and G. A. Abers (2006), Global compilation of variations in slab depth beneath arc volcanoes and implications, *Geochem. Geophys. Geosyst.*, *7*, Q05017, doi:10.1029/2005GC001045.
- Tassara, A. (2005), Interaction between the Nazca and South American plates and formation of the Altiplano-Puna plateau: Review of a flexural analysis along the Andean margin (15°–34°S), *Tectonophysics*, *399*, 39–57.
- Tassara, A., H.-J. Götze, S. Schmidt, and R. Hackney (2006), Three-dimensional density model of the Nazca plate and the Andean continental margin, *J. Geophys. Res.*, *111*, B09404, doi:10.1029/2005JB003976.
- Tassara, A., C. Swain, R. Hackney, and J. Kirby (2007), Elastic thickness structure of South America estimated using wavelets and satellite-derived gravity data, *Earth Planet. Sci. Lett.*, *253*(1–2), 17–36.
- Thompson, D. J. (1982), Spectrum estimation and harmonic analysis, *Proc. IEEE*, *70*, 1055–1096.
- Tovish, A., G. Schubert, and B. P. Luyendyk (1978), Mantle flow and the angle of subduction: Non-Newtonian corner flows, *J. Geophys. Res.*, *83*(B12), 5892–5898.
- van Hunen, J., A. P. van der Berg, and N. J. Vlaar (2004), Various mechanisms to induce present-day flat subduction and implications for the younger Earth: A numerical parameter study, *Phys. Earth Planet. Inter.*, *146*, 179–194.
- Vlaar, N. J. (1983), Thermal anomalies and magmatism due to lithospheric doubling and shifting, *Earth Planet. Sci. Lett.*, *65*, 322–330.
- Vlaar, N. J., and M. J. R. Wortel (1976), Lithospheric aging, instability and subduction, *Tectonophysics*, *32*, 331–351.
- von Huene, R., C. R. Ranero, and P. Vannucchi (2004), Generic model of subduction erosion, *Geology*, *32*(10), 913–916, doi:10.1130/G20563.1.
- Wagner, L. S., S. Beck, G. Zandt, and M. N. Ducea (2006), Depleted lithosphere, cold, trapped, and frozen melt puddles above the flat slab in central Chile and Argentina, *Earth Planet. Sci. Lett.*, *245*, 289–301.
- Watts, A. B. (2001), *Isostasy and Flexure of the Lithosphere*, Cambridge Univ. Press, New York.
- Watts, A. B., S. H. Lamb, J. D. Fairhead, and J. F. Dewey (1995), Lithospheric flexure and bending of the central Andes, *Earth Planet. Sci. Lett.*, *134*, 9–21.
- Whitman, D., B. L. Isacks, and S. Mahlburg Kay (1996), Lithospheric structure and along-strike segmentation of the Central Andean Plateau: Seismic Q, magmatism, flexure, topography and tectonics, *Tectonophysics*, *259*, 29–40.
- Yáñez, G., and J. Cembrano (2004), Role of viscous plate coupling in the late Tertiary Andean tectonics, *J. Geophys. Res.*, *109*, B02407, doi:10.1029/2003JB002494.
- Yáñez, G., C. R. Ranero, R. von Huene, and J. Díaz (2001), Magnetic anomaly interpretation across the southern central Andes (32°–34°): The role of the Juan Fernández Ridge in the late Tertiary evolution of the margin, *J. Geophys. Res.*, *106*, 6325–6345.
- Yuan, X., S. V. Sobolev, and R. Kind (2002), Moho topography in the central Andes and its geodynamic implications, *Earth Planet. Sci. Lett.*, *199*, 389–402.